


Article

Supercilious Enhancement in Oxygen-Reduction Catalytic Functionalities of Cubic Perovskite Structured LaFeO_3 by Co-Doping of Gd and Ce for LT-SOFCs

Jinpeng Li ¹, Naveed Mushtaq ² , M.A.K. Yousaf Shah ² , Yuzheng Lu ³ and Shun Yan ^{3,*}

¹ Department of Electronic Engineering, Huainan Union University, Huainan 232000, China

² Jiangsu Provincial Key Laboratory of Solar Energy Science and Technology/Energy Storage Joint Research Centre, School of Energy and Environment, Southeast University, No. 2 Si Pai Lou, Nanjing 210096, China

³ School of Electronic and Engineering, Nanjing Xiaozhuang University, Nanjing 211171, China

* Correspondence: 2019008@njxzc.edu.cn

Abstract: Low-temperature solid fuel cells (LT-SOFCs) hold remarkable promise for the cooperative corporation of small- and large-scale applications. However, the meager oxygen-reduction retort of cathode materials mires the low operating temperature conditions of SOFCs. Herein, we have developed a perovskite structured LaFeO_3 by the co-doping of Gd and Ce ions, and their electrochemical properties have been studied. The developed $\text{LaFe}_{0.8}\text{Gd}_{0.1}\text{Ce}_{0.1}\text{O}_{3-\delta}$ cathode exhibits very small-area-specific-resistance and good oxygen-reduction reaction (ORR) activity at low operating temperatures of 450–500 °C. We have demonstrated a high-power density of $0.419 \text{ W}\cdot\text{cm}^{-2}$ with a $\text{LaFe}_{0.8}\text{Gd}_{0.1}\text{Ce}_{0.1}\text{O}_{3-\delta}$ cathode operating at 550 °C with H_2 and atmospheric air as fuels. Moreover, $\text{LaFe}_{0.8}\text{Gd}_{0.1}\text{Ce}_{0.1}\text{O}_{3-\delta}$ exhibits high activation energy as compared to individual LaFeO_3 , which helps to promote ORR activity. Various spectroscopic measurements such as X-ray diffraction, SEM, EIS, UV-visible, TGA, Ramana, and photoelectron spectroscopy were employed to understand the improved ORR electrocatalytic activity of Gd and Ce co-doped LaFeO_3 cathode. The results can further help to develop functional cobalt-free electro-catalysts for LT-SOFCs.

Keywords: perovskite structured LaFeO_3 ; Gd and Ce co-doped; $\text{LaFe}_{0.8}\text{Gd}_{0.1}\text{Ce}_{0.1}\text{O}_{3-\delta}$; electrochemical properties; spectroscopic studies; LT-SOFCs cathode



Citation: Li, J.; Mushtaq, N.; Yousaf Shah, M.; Lu, Y.; Yan, S. Supercilious Enhancement in Oxygen-Reduction Catalytic Functionalities of Cubic Perovskite Structured LaFeO_3 by Co-Doping of Gd and Ce for LT-SOFCs. *Crystals* **2023**, *13*, 242. <https://doi.org/10.3390/cryst13020242>

Academic Editor: Dmitry Medvedev

Received: 26 October 2022

Revised: 22 December 2022

Accepted: 18 January 2023

Published: 31 January 2023



Copyright: © 2023 by the authors. Licensee MDPI, Basel, Switzerland. This article is an open access article distributed under the terms and conditions of the Creative Commons Attribution (CC BY) license (<https://creativecommons.org/licenses/by/4.0/>).

1. Introduction

Solid oxide fuel cells (SOFCs) are efficient and clean energy devices in power-generation systems and have been long-standing investigated as potential conversion tools. However, high operating temperature, low ionic conductivity, long-term startup, and sluggish oxygen-reduction reaction (ORR) kinetics act as stumbling blocks toward SOFCs commercialization. Cathode one of the key components readily hampers the electrochemical performance when it comes to operating fuel cells at low operating temperatures due to poor catalytic functionalities [1–5]. These challenges at low operating temperatures can be mitigated by using advanced fabrication technology or by developing high-performing cathodes via structural and surface modification [6]. These approaches lead to lowering the operating temperatures of SOFCs to 300–600 °C, which can significantly increase the number of applications of LT-SOFC technology and facilitate material selection with greater reliability [7].

High-performing cathode materials with enhanced mixed ionic and electronic conduction, along with low electrode polarization and fast ORR functionalities, are the utmost key requirement for the development of LT-SOFCs. In this regard, diverse strategies have been reported to improve electrochemical performance at low operating temperatures. Zhang et al. achieved polarization resistance of $0.394 \Omega \text{ cm}^2$ by introducing ionic conductor $\text{Gd}_{0.1}\text{Ce}_{0.9}\text{O}_{2-\delta}$ into $\text{PrBaCo}_2\text{O}_{5+\delta}$ via surface modification [8,9]. Several other studies focus on material selection and found the perovskite cathode to be an efficient

electrode with enhanced ORR kinetics at low temperatures $<600\text{ }^{\circ}\text{C}$. Perovskite cathode $\text{Ba}_{0.5}\text{Sr}_{0.5}\text{Co}_{0.8}\text{Fe}_{0.2}\text{O}_{3-\delta}$ delivers a peak power density of 454 mW cm^{-2} at $500\text{ }^{\circ}\text{C}$, higher than the conventional cathode $\text{La}_{0.6}\text{Sr}_{0.4}\text{Co}_{0.2}\text{Fe}_{0.8}\text{O}_{3-\delta}$ and the $\text{Sm}_{0.5}\text{Sr}_{0.5}\text{CoO}_{3-\delta}$ cathode. The reported result clearly shows that structure modification and material selection play a key role in enhancing ORR kinetic at low temperatures [7]. The reason for high catalytic in Perovskite is that enriched oxygen vacancies at lattice due to defects in crystal structure on doping leads to improved ORR catalytic properties. Co- and Fe-based perovskite has shown astonishing fast catalytic functionality at low operating temperatures. Particularly, $\text{La}_x\text{Sr}_{1-x}\text{Co}_y\text{Fe}_{1-y}\text{O}_{3-\delta}$, $\text{Ba}_{0.5}\text{Sr}_{0.5}\text{Co}_{1-x}\text{Fe}_x\text{O}_{3-\delta}$, and $\text{BaCo}_x\text{Fe}_{1-x}\text{O}_{3-\delta}$ deliver exceptionally low polarization resistance in comparison to conventional cathode pure Fe-based cathode material [10,11]. Although, the presence of cobalt in the perovskite cathode has shown high performance, it undergoes poor structural stability and exhibits large thermal expansion coefficients and limiting ORR functionalities, particularly when the SOFC operate at low temperatures [12–14]. Therefore, the development of Co-free or replacing Cobalt with any other efficient element can gain considerable attention, due to their stability in an oxidizing atmosphere and improved electrocatalytic functionalities towards ORR [15].

From the reported literature, it can be perceived that either by surface modification or using structural changes, the performance and stability of the $\text{LaFeO}_{3-\delta}$ cathode by Gd and Ce doping are improved. Therefore, in this work, we dope ionic conductors doping of Gd and Ce in LaFeO_3 and use them as cathode materials in LT-SOFCs. LFGdCeO_3 cathode materials are characterized and investigated in terms of a crystal structure along with the analysis of surface and interface properties, followed by being applied in SOFC to investigate I-V & I-P performance and EIS. It is found that $\text{LaFe}_{0.8}\text{Gd}_{0.1}\text{Ce}_{0.1}\text{O}_{3-\delta}$ delivers minimum electrode polarization resistance along with high power density of 0.419 Wcm^{-2} at the low temperature of $550\text{ }^{\circ}\text{C}$. Additionally, various spectroscopic analyses show that the configured SOFC cathode is a persistently good candidate for depicting fast catalytic functionality and chemical stability in an oxidizing atmosphere.

2. Materials and Methods

2.1. Synthesis Procedures

Gd and Ce-doped LaFeO_3 perovskite structured residues were made via a sol-gel method using citric acid and ethylenediaminetetraacetic acid (EDTA) as complexing agents. In the first step, 0.1 moles of EDTA were dissolved in de-ionized H_2O , and subsequently, ammonia solution was added into the solution to set the pH of the to 7.0 and make the solution transparent. Next, suitable amounts of $\text{La}(\text{NO}_3)_3 \cdot 6\text{H}_2\text{O}$, $\text{Fe}(\text{NO}_3)_3 \cdot 9\text{H}_2\text{O}$, $\text{Gd}(\text{NO}_3)_3 \cdot 9\text{H}_2\text{O}$, and $\text{Ce}(\text{NO}_3)_3 \cdot 9\text{H}_2\text{O}$ bought from Alfa Aesar with 99.98% purity were detached into the solution. Afterward, 0.1 mole of citric acid was added in the above prepared solution. After that, the solution was continuously stirred at 240 rpm at $80\text{ }^{\circ}\text{C}$ for 10 h, and as a result, a $\text{LaFe}_{0.8}\text{Gd}_{0.1}\text{Ce}_{0.1}\text{O}_{3-\delta}$ brownish gel was obtained from the solution. In the next step, the obtained brownish gel was dried at $140\text{ }^{\circ}\text{C}$ in an oven. Finally, the dried gel was ground and calcinated at $950\text{ }^{\circ}\text{C}$ for 6 h in air. The pure LaFeO_3 and $\text{LaFe}_{0.9}\text{Gd}_{0.05}\text{Ce}_{0.05}\text{O}_{3-\delta}$ were prepared using same protocols for comparative study.

2.2. Characterizations Tools and Electrochemical Measurements

Bruker D8 with $\text{Cu-K}\alpha$ radiation ($\lambda = 1.5418\text{ \AA}$) was used to measure the X-ray diffraction pattern of LaFeO_3 , $\text{LaFe}_{0.9}\text{Gd}_{0.05}\text{Ce}_{0.05}\text{O}_{3-\delta}$, and $\text{LaFe}_{0.8}\text{Gd}_{0.1}\text{Ce}_{0.1}\text{O}_{3-\delta}$. Merlin compacts (Zeiss) were used to perform scanning electron microscopy (SEM). Surface analysis of the LaFeO_3 and $\text{LaFe}_{0.8}\text{Gd}_{0.1}\text{Ce}_{0.1}\text{O}_{3-\delta}$ was performed using X-ray photoelectron spectroscopy (Physical Electronics Quantum 2000) with an $\text{Al K}\alpha$ X-ray source at room temperature in ultra-high vacuum (UHV). XPS analysis was performed using Peak 41. The UV-visible absorption was measured using a UV-Vis 3600 spectrophotometer. The Gamry Reference 3000, USA workstation was used to measure electrochemical impedance spectroscopy (EIS) under the open-circuit voltage (OCV) with 10 mV of dc signal over the

frequency range of 0.1 to 106 Hz. The recorded data were analyzed using ZSIMPWIN software to obtain the EIS data.

2.3. Complete Fabrication of Fuel Cells

Our aim was to study the practical applicability of the Gd, Ce co doping in LaFeO_3 , and $\text{LaFe}_{0.8}\text{Gd}_{0.05}\text{Ce}_{0.05}\text{O}_{3-\delta}$ and $\text{LaFe}_{0.8}\text{Gd}_{0.1}\text{Ce}_{0.2}\text{O}_{3-\delta}$ as air electrodes in SOFC over $\text{Gd}_{0.1}\text{Ce}_{0.9}\text{O}_2$ (GDC) and $\text{Ni}_{0.8}\text{Co}_{0.15}\text{Al}_{0.05}\text{LiO}_{2-\delta}$ (NCAL-Ni-foam) anodes. The fuel cells were prepared by the dry pressing method. In first step, $\text{Ni}_{0.8}\text{Co}_{0.15}\text{Al}_{0.05}\text{LiO}_{2-\delta}$ was mixed with terpinol and painted on a porous Ni-foam substrate. The as-prepared LaFeO_3 , $\text{LaFe}_{0.8}\text{Gd}_{0.05}\text{Ce}_{0.05}\text{O}_{3-\delta}$, and $\text{LaFe}_{0.8}\text{Gd}_{0.1}\text{Ce}_{0.2}\text{O}_{3-\delta}$ were used as air electrode and Ni-foam $\text{Ni}_{0.8}\text{Co}_{0.15}\text{Al}_{0.05}\text{LiO}_{2-\delta}$ (NCAL-Ni-foam) from Bamo Sci. and Tech. Joint Stock Ltd. as a fuel electrode (anode) prepared by the same method. In the next step, one piece of Ni-foam NCAL was placed in a steel mould followed by $\text{Sm}_{0.2}\text{Ce}_{0.8}\text{O}_{2-\delta}$ (SDC) electrolyte powders (0.20 g) and $\text{LaFe}_{0.8}\text{Gd}_{0.1}\text{Ce}_{0.2}\text{O}_{3-\delta}$ powders and pressed at 220 MPa to obtain three-layer devices. All types of fuel cells were fabricated using the same protocol. Afterwards, the prepared fuel cell devices were heated at 600°C for 4 h in Ar to obtain a dense electrolyte layer (\cong relative density of 92%) to avoid gas leakage. Furthermore, a symmetrical cell with $\text{LaFe}_{0.8}\text{Gd}_{0.1}\text{Ce}_{0.2}\text{O}_{3-\delta}$ electrodes over the SDC electrolyte was fabricated for ORR activity measurements. The active area of all the devices was 0.64 cm². The performance demonstration of single cells was performed with 3% H₂O humidified hydrogen fuel and air from the atmosphere as oxidants. The drift rates of H₂/air were set to approximately 100–120 \pm 5% mL/min.

3. Results

3.1. Structure and Composition Analysis

Figure 1a shows the XRD pattern LaFeO_3 , $\text{LaFe}_{0.9}\text{Gd}_{0.05}\text{Ce}_{0.05}\text{O}_{3-\delta}$, and $\text{LaFe}_{0.8}\text{Gd}_{0.1}\text{Ce}_{0.2}\text{O}_{3-\delta}$ in the 2 θ range from 10–90°. The central peaks of the LaFeO_3 diffraction pattern are located at 23, 32, 39, 46, 57, 68, and 76, which can be indexed to the (100), (110), (111), (200), (211), (220), and (310) planes, respectively, of the cubic structure, with space group pm-3m (221) and a lattice of $a = b = c = 3.94$ and $\alpha = \beta = \gamma = 90^\circ$ [16]. Moreover, Figure 1b shows the comparative diffraction pattern of LaFeO_3 , $\text{LaFe}_{0.9}\text{Gd}_{0.05}\text{Ce}_{0.05}\text{O}_{3-\delta}$, and $\text{LaFe}_{0.8}\text{Gd}_{0.1}\text{Ce}_{0.2}\text{O}_{3-\delta}$ in the 2 θ range from 30–37° where the dominant diffraction peaks of $\text{La}_{0.1}\text{Sr}_{0.9}\text{Co}_{0.9}\text{Ce}_{0.1}\text{O}_{3-\delta}$ and $\text{La}_{0.2}\text{Sr}_{0.8}\text{Co}_{0.8}\text{Ce}_{0.2}\text{O}_{3-\delta}$ at 2 θ of 32° shift towards a lower angle, possibly because of the high ionic radius of Gd³⁺ and Ce^{4+/3+} ion [17,18].

Figure 2a–f shows the microscopic SEM image of $\text{LaFe}_{0.8}\text{Gd}_{0.1}\text{Ce}_{0.1}\text{O}_{3-\delta}$ at a different scale. The morphology of $\text{LaFe}_{0.9}\text{Gd}_{0.05}\text{Ce}_{0.05}\text{O}_{3-\delta}$ is shown to be very fine and nano-structured. The $\text{LaFe}_{0.9}\text{Gd}_{0.05}\text{Ce}_{0.05}\text{O}_{3-\delta}$ shows the particle size of about 50 nm. Figure 2a–f shows the SEM image of $\text{LaFe}_{0.9}\text{Gd}_{0.05}\text{Ce}_{0.05}\text{O}_{3-\delta}$, where a highly porous structure can be seen, while Figure 3b–f shows the EDS mapping image of $\text{LaFe}_{0.8}\text{Gd}_{0.1}\text{Ce}_{0.1}\text{O}_{3-\delta}$ of SEM image in Figure 3a. The EDS mapping image of the chemical distribution of each element in $\text{LaFe}_{0.8}\text{Gd}_{0.1}\text{Ce}_{0.1}\text{O}_{3-\delta}$ can clearly be seen. The elemental mapping image with mixed colors was used to reveal the chemical distribution by energy dispersive spectroscopy (EDS), where the homogenous chemical concentration of each element such as La, Fe, Gd, Ce, and O can be identified [19]. Moreover, the mapping of the chemical distribution of each element individually is shown in Figure 3c–f measured using SEM image in Figure 3a, which could help estimate the chemical distribution [20,21]. Moreover, Figure 3g shows the EDS spectrum of the $\text{LaFe}_{0.8}\text{Gd}_{0.1}\text{Ce}_{0.1}\text{O}_{3-\delta}$ sample, which could help one to understand the actual chemical composition of the powder.

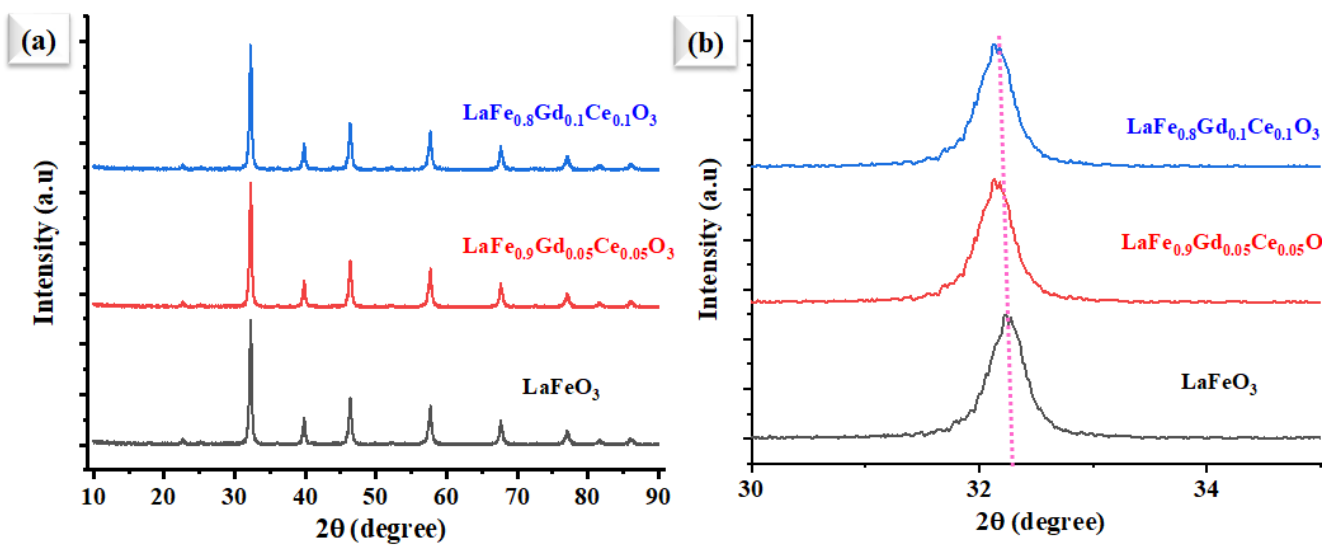


Figure 1. (a) measured X-ray diffraction pattern of LaFeO_3 , $\text{LaFe}_{0.9}\text{Gd}_{0.05}\text{Ce}_{0.05}\text{O}_{3-\delta}$, and $\text{LaFe}_{0.8}\text{Gd}_{0.1}\text{Ce}_{0.1}\text{O}_{3-\delta}$, respectively. (b) Comparison of peak shifting of LaFeO_3 with Gd and Ce doping.

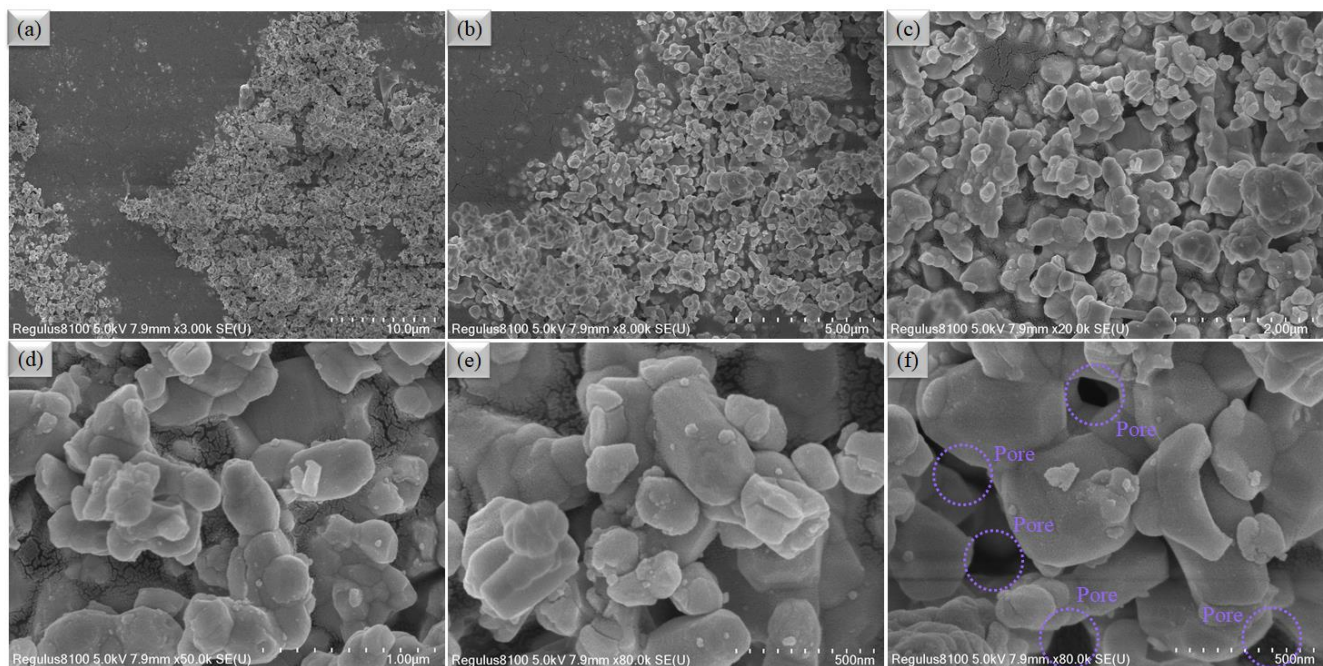


Figure 2. (a–f) The surface morphology studied by SEM for $\text{LaFe}_{0.8}\text{Gd}_{0.1}\text{Ce}_{0.1}\text{O}_{3-\delta}$ powder at different scale of 10–500 nm.

3.2. Electrochemical Impedance and Electrical Conductivity

The cathodic polarization contributes the most to the entire impedance spectra of SOFCs. Hence it is necessary to understand and determine the cathodic polarization process and the rate-determining step involved in ORR activity and slow down it. To study the ORR properties of $\text{LaFe}_{0.8}\text{Gd}_{0.1}\text{Ce}_{0.1}\text{O}_{3-\delta}$ in a symmetrical cell over SDC electrolyte, EIS characterization was carried out using the electrochemical impedance spectroscopy as shown in Figure 4. The EIS was measured symmetrical cells in air at 400–550 °C, under OCV conditions. A comparison of the Nyquist plots of $\text{La}_{0.2}\text{Sr}_{0.8}\text{Co}_{0.8}\text{Ce}_{0.2}\text{O}_{3-\delta}$ embedded on porous Ni-foam cells over an SDC electrolyte obtained from EIS data at different operating temperatures of 550–425 °C is shown in Figure 4a–f. The model circuit $R_o - (R_g - CPE_1) - (R_{gb} - CPE_2)$ that fits the EIS results suggests a very low charge and mass transport resistance for the $\text{LaFe}_{0.8}\text{Gd}_{0.1}\text{Ce}_{0.1}\text{O}_{3-\delta}$ cathode at 550 °C, as shown in

Figure 4a [22,23]. The fitted data describe two dominant polarization losses signified by the ASR at LF (low frequencies) and HF (high frequencies) [22–25]. Since ORR is described as a multistep process, such as (i) the surface adsorption/gas diffusion and separation of O_2 from air; (ii) the diffusion of O_{ad} ; (iii) the conversion of absorbed O_2 into O_{2-} ; and (iv) the transportation of O^{2-} to the cathode/electrolyte interface. A step-by-step or parallel combination of these processes could be involved [26–28]. However, low ASR in the $LaFe_{0.8}Gd_{0.1}Ce_{0.1}O_{3-\delta}$ cathode could be the parallel combination of these steps. The large grain boundary in the single-phase cathode materials plays a significant role in slowing down the ORR process. The very-low-charge transport resistance of $0.04 \Omega cm^2$ is trialed, whereas the resistance of mass transport is $0.32 \Omega cm^2$. Most often, oxygen vacancies are virtually studied in simply doped oxide materials at low temperatures of interest for applications [29], while the co-doping of Gd and Ce to form $LaFe_{0.8}Gd_{0.1}Ce_{0.1}O_{3-\delta}$ can be applied to enhance ORR activity and TPBs for developing the SOFCs cathode. In addition, electrochemical impedance analysis indicates that the surface exchange process of oxygen is more dominant than the bulk diffusion process of oxygen in $LaFe_{0.8}Gd_{0.1}Ce_{0.1}O_{3-\delta}$.

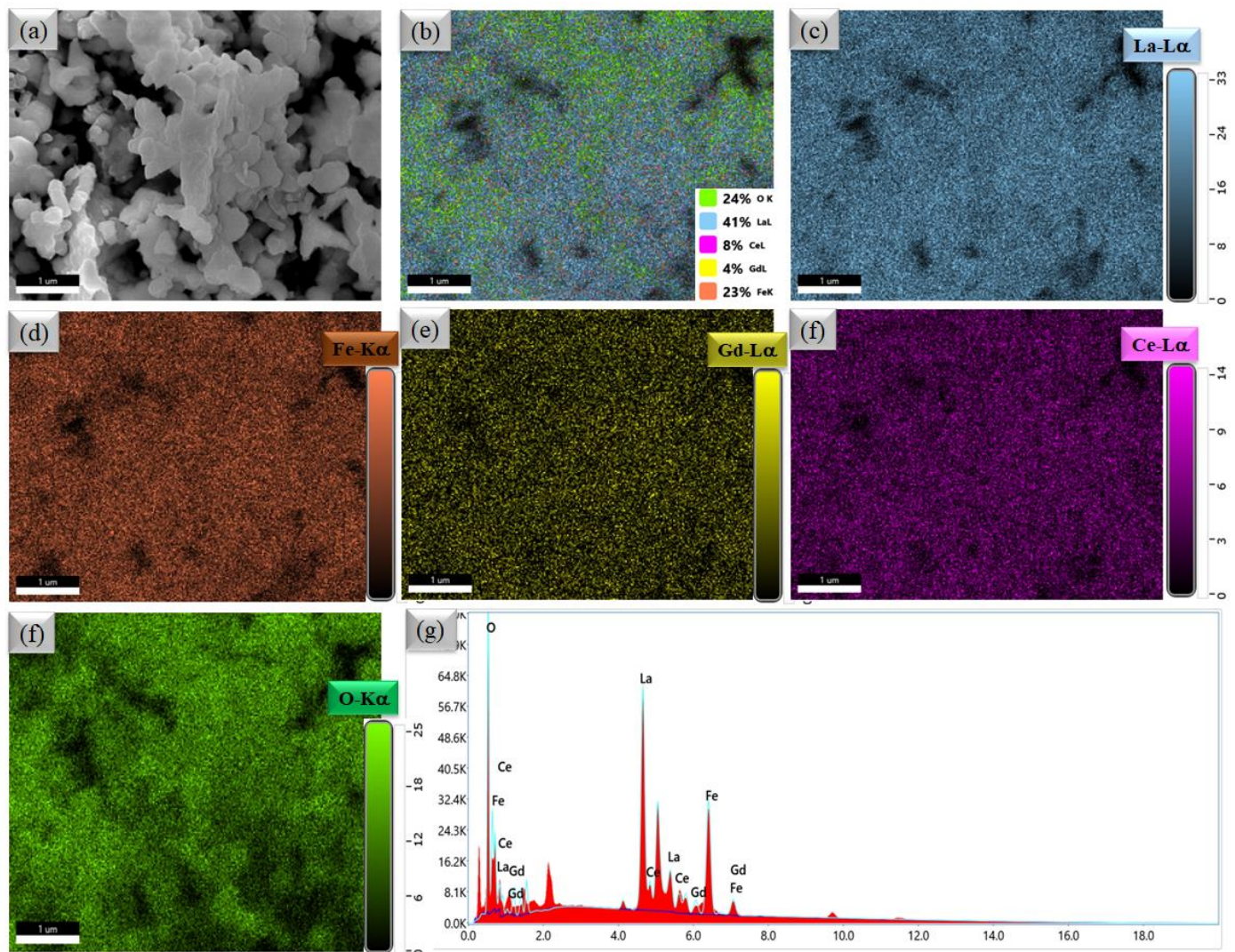


Figure 3. (a) The surface morphology studied by SEM for $LaFe_{0.8}Gd_{0.1}Ce_{0.1}O_{3-\delta}$ powders; (b–f) combined and individual EDS mapping image of La, Fe, Gd, Ce, and O in $LaFe_{0.9}Gd_{0.05}Ce_{0.05}O_{3-\delta}$ of SEM image in (a); and (g) EDS spectrum of $LaFe_{0.8}Gd_{0.1}Ce_{0.1}O_{3-\delta}$.

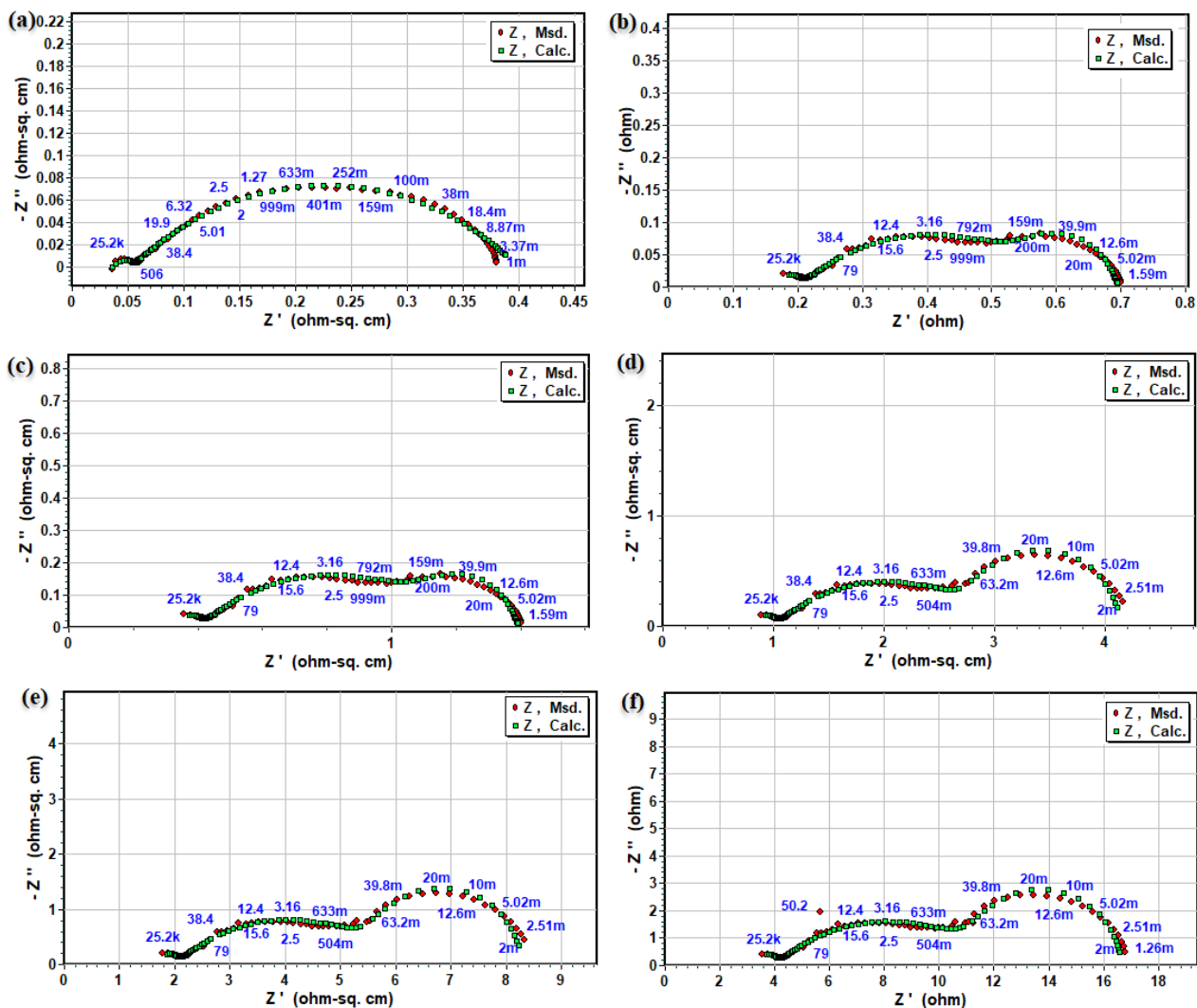


Figure 4. (a–f) Nyquist plot of impedance spectra for symmetrical $\text{LaFe}_{0.8}\text{Gd}_{0.1}\text{Ce}_{0.1}\text{O}_{3-\delta}$ electrode cell cathode over SDC electrolyte different operating temperatures of 550 °C, 525 °C, 500 °C, 475 °C, 450 °C, and 425 °C, respectively.

3.3. Electrochemical Performance Measurements

The electrochemical performance of the prepared LaFeO_3 , $\text{LaFe}_{0.9}\text{Gd}_{0.05}\text{Ce}_{0.05}\text{O}_{3-\delta}$, and $\text{LaFe}_{0.8}\text{Gd}_{0.1}\text{Ce}_{0.1}\text{O}_{3-\delta}$ as air electrodes was demonstrated in SOFC at 550 °C over the SDC electrolyte. Figure 5c displays a typical current (I)–voltage (V) and I-P characteristics curve of fabricated fuel cells. An OCV of over 1.1 V and the maximum power density (P_{max}) of 0.419 W cm^{-2} using the $\text{LaFe}_{0.8}\text{Gd}_{0.1}\text{Ce}_{0.1}\text{O}_{3-\delta}$ cathode were compared to using LaFeO_3 , P_{max} of 0.245 W cm^{-2} (Figure 5a) and P_{max} of 0.338 W cm^{-2} (Figure 5b) for $\text{LaFe}_{0.9}\text{Gd}_{0.05}\text{Ce}_{0.05}\text{O}_{3-\delta}$ cathodes, respectively at 550 °C. The high electrochemical performance achieved by the $\text{LaFe}_{0.8}\text{Gd}_{0.1}\text{Ce}_{0.1}\text{O}_{3-\delta}$ cathode over individual LaFeO_3 and $\text{LaFe}_{0.9}\text{Gd}_{0.05}\text{Ce}_{0.05}\text{O}_{3-\delta}$ samples suggests co-doping of Gd and Ce and plays an essential role in improving ORR electrocatalytic activity by leading lower barrier O^{2-} transport and its migration energy [12,17] since the catalytic process at the cathode surface is a multi-step process, and the $\text{LaFe}_{0.9}\text{Gd}_{0.05}\text{Ce}_{0.05}\text{O}_{3-\delta}$ could be enriched with oxygen vacancies, which would enhance the capability of capturing valance electrons to improve the electrical conductivity as well. Moreover, the cross-sectional SEM of the fuel cell using the $\text{LaFe}_{0.9}\text{Gd}_{0.05}\text{Ce}_{0.05}\text{O}_{3-\delta}$ cathode over the GDC cathode after fuel-cell testing is performed to the individual layer in the cell components, as shown in Figure 5d.

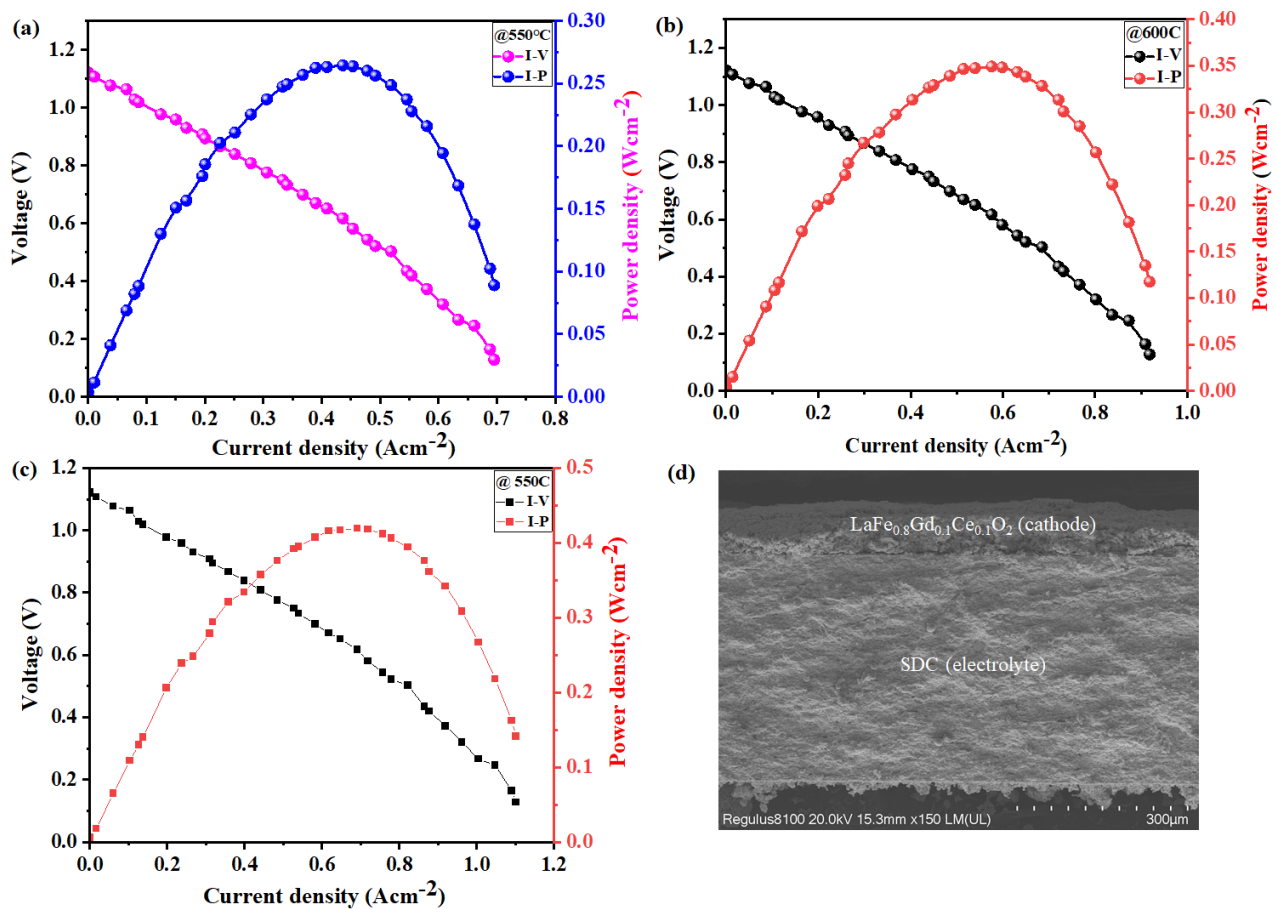


Figure 5. (a–c) Electrochemical performances: characteristic curves of utilizing our LaFe_{0.8}Gd_{0.1}Ce_{0.1}O_{3-δ} when comparing LaFeO₃ and LaFe_{0.9}Gd_{0.05}Ce_{0.05}O_{3-δ} cathodes in fuel cells over SDC electrolyte and NCAL-Ni-foam anode operated at 550 °C (d) cross-sectional SEM images of tri-layer electrolyte supported fuel cell along with prepared LaFe_{0.8}Gd_{0.1}Ce_{0.1}O_{3-δ} cathode and SDC electrolyte examined after the electrochemical test.

3.4. Spectroscopic Analysis

Additionally, a wide range of spectroscopic methods, including UV–visible, TGA, Raman, and X-ray photoelectron spectroscopy, were used to investigate additional structural characteristics of LaFeO₃ and Gd/Ce co-doped LaFeO₃ powders. Figure 6a shows the absorbance spectra of pure LaFeO₃ and LaFe_{0.8}Gd_{0.1}Ce_{0.1}O_{3-δ} measured by UV–visible spectroscopy. It is possible to see a substantial difference in the absorbance spectra of the as-synthesized LaFeO₃ and LaFe_{0.8}Gd_{0.1}Ce_{0.1}O_{3-δ} powders. The variations in the absorbance spectra indicate that the LaFeO_{3-δ} energy band gap is lowered with the doping of Gd and Ce; this is only possible because of the creation of oxygen vacancies. This is widely reported when a large number of oxygen vacancies are produced, which also reduce the metal oxides' energy band gaps [30,31].

Moreover, the TGA was conducted in air at 30 to 800 °C to further investigate the thermal effects of the Gd and Ce doping on the LaFeO₃ particles, as demonstrated in Figure 6b. The evaporation of the absorbed water is indicated by the rapid weight loss in both samples around 100 °C. The rapid weight changes begin at around 300 °C for the LaFe_{0.8}Gd_{0.1}Ce_{0.1}O_{3-δ} powders, while the other rapid weight changes start at 500–600 °C to release lattice oxygen in the form of oxygen vacancies. The LaFe_{0.8}Gd_{0.1}Ce_{0.1}O_{3-δ} sample exhibits the highest mass change, which is fully evident and supports our hypotheses. The large mass change in LaFe_{0.8}Gd_{0.1}Ce_{0.1}O_{3-δ} could be released easily because of the softening of the O bands when Gd and Ce are doped in LaFeO₃.

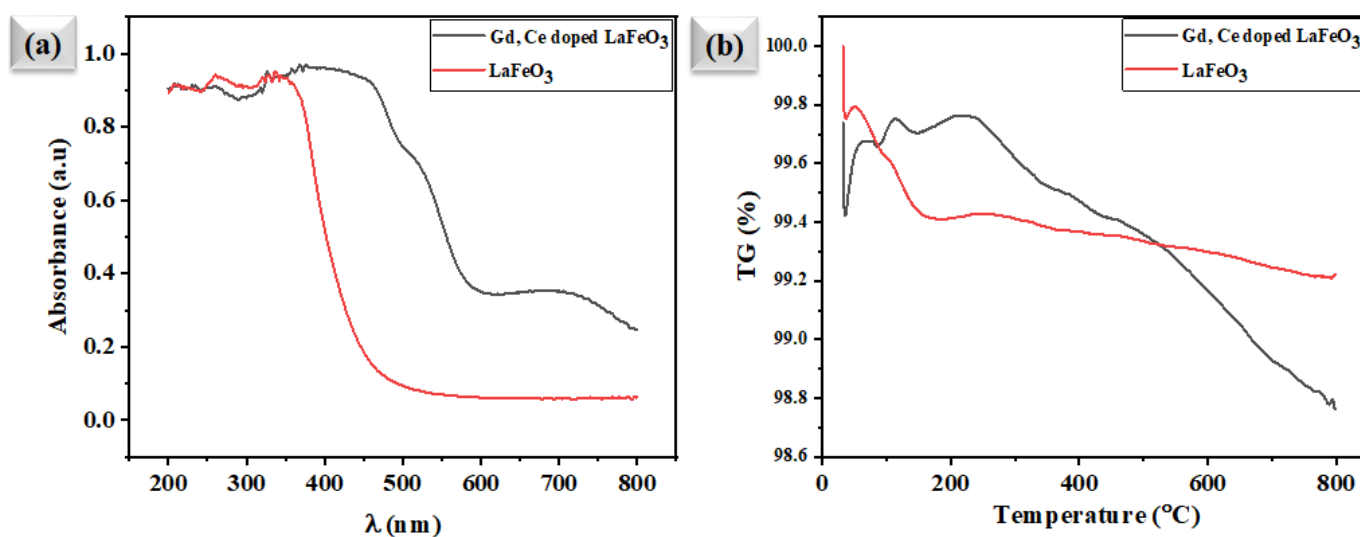


Figure 6. (a) The UV-visible spectra of LaFeO_3 and $\text{LaFe}_{0.8}\text{Gd}_{0.1}\text{Ce}_{0.1}\text{O}_{3-\delta}$ and (b) thermogravimetric analysis of LaFeO_3 and $\text{LaFe}_{0.8}\text{Gd}_{0.1}\text{Ce}_{0.1}\text{O}_{3-\delta}$ cathode, respectively.

Figure 7a shows the Raman spectroscopy of $\text{LaFe}_{0.8}\text{Gd}_{0.1}\text{Ce}_{0.1}\text{O}_{3-\delta}$ in comparison with LaFeO_3 . The specific Raman bands of LaFeO_3 and $\text{LaFe}_{0.8}\text{Gd}_{0.1}\text{Ce}_{0.1}\text{O}_{3-\delta}$ are centered at 220, 463, and 1310 cm^{-1} , respectively. However, a down-shift in the bands was observed for the $\text{LaFe}_{0.8}\text{Gd}_{0.1}\text{Ce}_{0.1}\text{O}_{3-\delta}$ sample. Typically, the down-shift in the $\text{LaFe}_{0.8}\text{Gd}_{0.1}\text{Ce}_{0.1}\text{O}_{3-\delta}$ peak causes a decrease in energy when exciting the vibrations along gradually looser bonds in the presence of $\text{LaFe}_{0.8}\text{Gd}_{0.1}\text{Ce}_{0.1}\text{O}_{3-\delta}$. It confirms that the high ORR activity could result after loose oxygen bonding at the interface of $\text{LaFe}_{0.8}\text{Gd}_{0.1}\text{Ce}_{0.1}\text{O}_{3-\delta}$, hence resulting in high densities of active surface-oxygen species to enhance ORR electrocatalytic activity.

Figure 7b–f shows the high-resolution XPS spectra for the individual elements in $\text{LaFe}_{0.8}\text{Gd}_{0.1}\text{Ce}_{0.1}\text{O}_{3-\delta}$ before and after doping, where the change in oxidation state of each element such as Fe, Ce, and O1s can clearly be observed after dispersing doping of Gd and Ce. After subtracting Shirley's background, high-resolution XPS spectra were fitted by a mixture of Lorentzian and Gaussian function. Our focus was to observe the chemical and electronic state configuration changes of Fe-2p (Figure 7b,c), Ce-3d (Figure 7d,e), and O 1s (Figure 7f) spectra, respectively. The change in the chemical state of each element can be observed after Gd and Ce doping to pristine LaFeO_3 materials. The Fe^{4+} -2p_(3/2, 1/2) and Fe^{3+} -2p_(3/2, 1/2) peaks in LaFeO_3 appear at 713.2/723.6 eV and 711.85/724.63 \pm 0.02 eV, whereas in $\text{LaFe}_{0.8}\text{Gd}_{0.1}\text{Ce}_{0.1}\text{O}_{3-\delta}$ they are at 712.25/723.73 and 709.58/724.93 \pm 0.02 eV, showing a binding energy up shift of 0.8 \pm 0.02 eV [32,33], signifying a down-shift of 0.5 \pm 0.05 eV to lower binding energy (B.E.). Figure 7d, e shows the XPS spectra of Ce-3d of the $\text{LaFe}_{0.9}\text{Gd}_{0.05}\text{Ce}_{0.05}\text{O}_{3-\delta}$ and $\text{LaFe}_{0.8}\text{Gd}_{0.1}\text{Ce}_{0.1}\text{O}_{3-\delta}$ samples. The Ce^{4+} and Ce^{3+} peaks of the $\text{LaFe}_{0.8}\text{Gd}_{0.1}\text{Ce}_{0.1}\text{O}_{3-\delta}$ sample appear at 881.82/900.65 eV and 898.45/915.72 eV, whereas for pure the $\text{LaFe}_{0.9}\text{Gd}_{0.05}\text{Ce}_{0.05}\text{O}_{3-\delta}$ sample they are at 882.152/901.65 and 899.32/916.45 eV [16], showing a significant change in a binding energy shift up to about 0.6 \pm 0.05 eV for the $\text{LaFe}_{0.8}\text{Gd}_{0.1}\text{Ce}_{0.1}\text{O}_{3-\delta}$ sample [34,35]. However, Fe-2p (3/2, 1/2) shows a down-shift in B.E., while the Ce-3d spectra shifts up to exhibit more mixed valence states, which help to create extra oxygen vacancies by maintaining charge-neutrality due to a difference in the electro negativity after dispersing the $\text{LaFe}_{0.8}\text{Gd}_{0.1}\text{Ce}_{0.1}\text{O}_{3-\delta}$ sample at porous Ni-foam [36–38].

The O1s spectrum of the $\text{La}_{0.2}\text{Sr}_{0.8}\text{Co}_{0.8}\text{Ce}_{0.2}\text{O}_{3-\delta}$ sample contains lattice oxygen (lattice O^{2-}) and oxygen vacancy ($\text{V}_{\text{O}}^{\bullet\bullet}$) peaks. The O1s spectra of the $\text{LaFe}_{0.8}\text{Gd}_{0.1}\text{Ce}_{0.1}\text{O}_{3-\delta}$ sample cathode material display two partially superimposed peaks (Figure 7f). There are two major excitations: the first includes O1s of the $\text{LaFe}_{0.8}\text{Gd}_{0.1}\text{Ce}_{0.1}\text{O}_{3-\delta}$ sample bands ranging from 528 to 533.5 eV. The low BE peak at 529.2 can be ascribed to the lattice oxygen (O Lattice), and the higher one at 531.4– to extra $\text{V}_{\text{O}}^{\bullet\bullet}$. The high area percentage ratio of Olat/Ovac of the

$\text{LaFe}_{0.8}\text{Gd}_{0.1}\text{Ce}_{0.1}\text{O}_{3-\delta}$ sample after the Gd and Ce doping cathode indicates its high oxygen-vacancy concentration and good oxygen-adsorption capability, which play an important role in high ORR activity [36,38]. The different steps involved in the ORR mechanism in the $\text{LaFe}_{0.8}\text{Gd}_{0.1}\text{Ce}_{0.1}\text{O}_{3-\delta}$ sample with the Ni-foam cathode are shown in Figure 8.

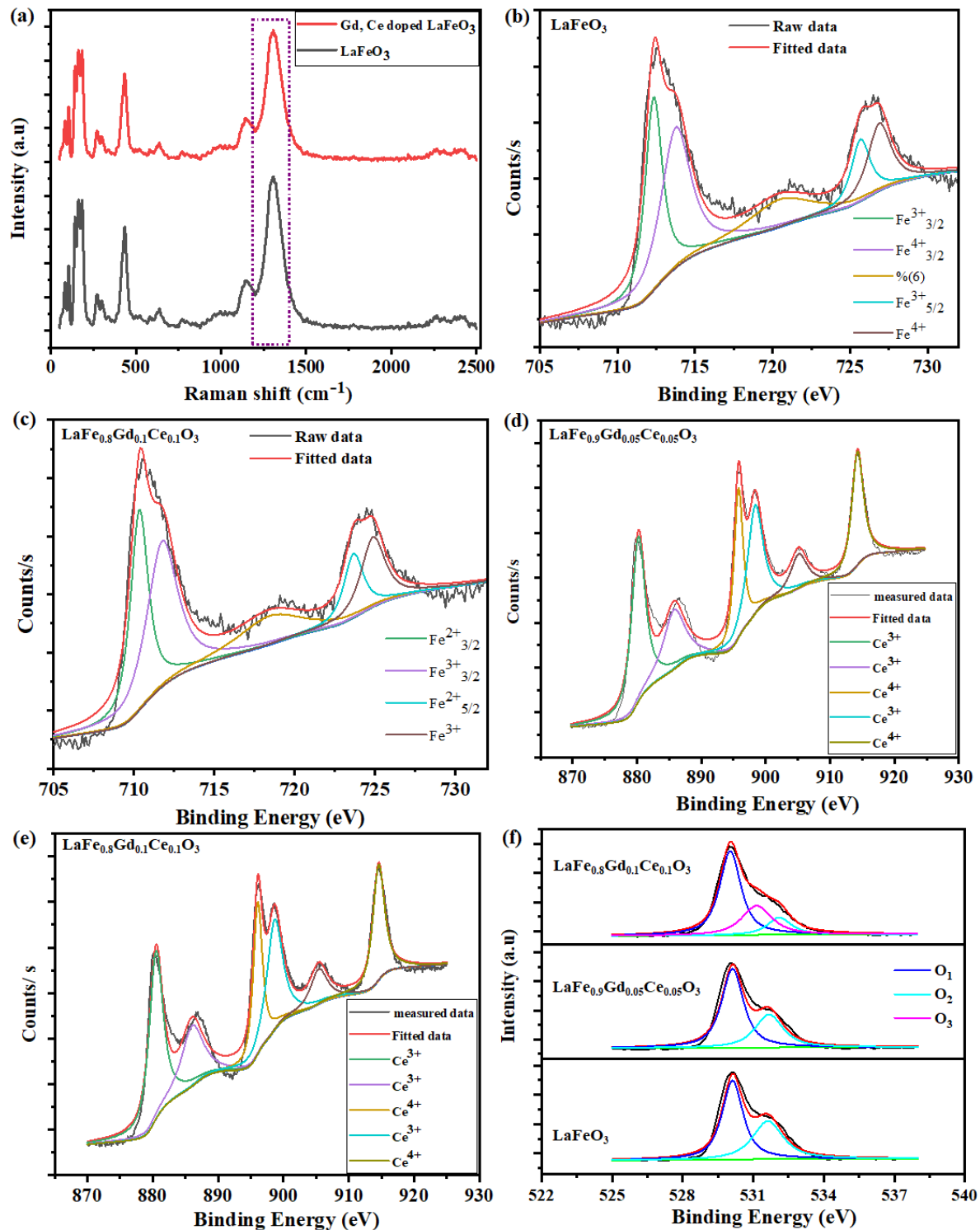


Figure 7. (a) Raman spectra of LaFeO_3 and $\text{LaFe}_{0.8}\text{Gd}_{0.1}\text{Ce}_{0.1}\text{O}_{3-\delta}$ (b,c) Fe-2p X-ray photoelectron spectra of $\text{LaFeO}_{3-\delta}$ individual powders and after doping of Gd and Ce to form $\text{LaFe}_{0.8}\text{Gd}_{0.1}\text{Ce}_{0.1}\text{O}_{3-\delta}$. (d,e) Ce-3d, XPS spectra of $\text{LaFe}_{0.9}\text{Gd}_{0.05}\text{Ce}_{0.05}\text{O}_{3-\delta}$ and $\text{LaFe}_{0.8}\text{Gd}_{0.1}\text{Ce}_{0.1}\text{O}_{3-\delta}$ sample and (f) O1s spectra, respectively.

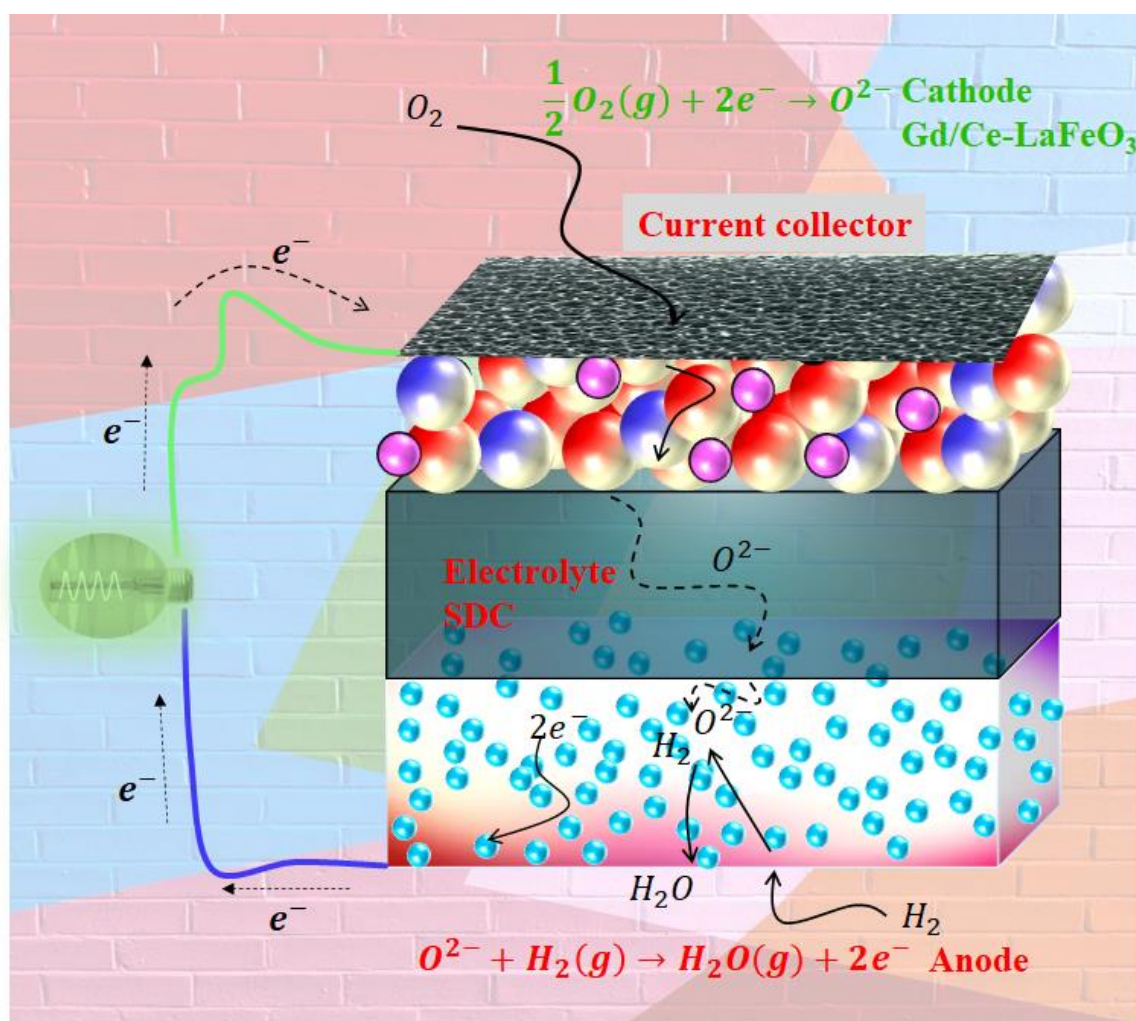


Figure 8. Schematic diagram of the different steps for electrochemical processes from fuel converting the fuel energy into electricity of Gd/Ce-doped LaFeO₃-based cathode fuel cell over SDC electrolyte.

4. Conclusions

In conclusion, in this work we have developed a semiconductor LaFeO₃ doped by both the A-site and B-site using Gd and ceria, respectively. Later, the developed Gd- and Ce-doped LaFeO₃ particles were used as air electrodes and their electrochemical properties were studied. The prepared LaFe_{0.9}Gd_{0.05}Ce_{0.05}O_{3-δ} and LaFe_{0.8}Gd_{0.01}Ce_{0.1}O_{3-δ} samples exhibit good ORR electrochemical performance at LTs, e.g., the maximum power density of 0.419 W cm^{−2} using a cathode over the SDC electrolyte at 550 °C. The excellent ORR electrocatalytic activity LaFe_{0.8}Gd_{0.01}Ce_{0.1}O_{3-δ} can be attributed to the porous structure obtained by the Gd and Ce doping into LaFeO₃. The mechanism for high electrochemical performance of LaFe_{0.8}Gd_{0.01}Ce_{0.1}O_{3-δ} is discussed in detail by different experimental approaches. The obtained results show that this approach could not be only useful in developing efficient ORR electrocatalysts but could also be applied to other relevant applications.

Author Contributions: The conceptualization of this work was completed by J.L. and N.M.; the methodology was completed by Y.L.; and formal analysis and investigation were completed by Y.L. and S.Y. The resources and data-curation facilities were provided by Y.L. and J.L. Original draft preparation was done by J.L. The review and editing were carried out by M.Y.S. and Y.L. All authors have read and agreed to the published version of the manuscript.

Funding: This work is supported the industry-University-Research Cooperation Project of Jiangsu in China (Grant No. BY2021057), and the Qing Lan Project of Jiangsu Province. This work is also partly

supported by the Jiangsu Province Higher Vocational College Young Teachers Enterprise Practice Training Funding Project (Grant No. 2021QYSJ048).

Data Availability Statement: The data that support the findings of this study are available from the corresponding authors upon reasonable request.

Acknowledgments: The authors would like to acknowledge the industry-University-Research Co-operation Project of Jiangsu Province in China (Grant No. BY2021057) for providing the funding to complete this work.

Conflicts of Interest: The authors declare no conflict of interest.

References

- Ormerod, R.M. Solid oxide fuel cells. *Chem. Soc. Rev.* **2003**, *32*, 17–28. [\[CrossRef\]](#) [\[PubMed\]](#)
- Jacobson, A.J. Materials for solid oxide fuel cells. *Chem. Mater.* **2010**, *22*, 660–674. [\[CrossRef\]](#)
- Pandey, A. Progress in solid oxide fuel cell (SOFC) research. *JOM* **2019**, *71*, 88–89. [\[CrossRef\]](#)
- Wachsman, E.D.; Lee, K.T. Lowering the temperature of solid oxide fuel cells. *Science* **2011**, *334*, 935–939. [\[CrossRef\]](#) [\[PubMed\]](#)
- Han, M.; Tang, X.; Yin, H.; Peng, S. Fabrication, microstructure and properties of a YSZ electrolyte for SOFCs. *J. Power Sources* **2007**, *165*, 757–763. [\[CrossRef\]](#)
- Leng, Y.; Chan, S.; Khor, K.; Jiang, S. Performance evaluation of anode-supported solid oxide fuel cells with thin film YSZ electrolyte. *Int. J. Hydrogen Energy* **2004**, *29*, 1025–1033. [\[CrossRef\]](#)
- Liu, Y.-L.; Hagen, A.; Barfod, R.; Chen, M.; Wang, H.-J.; Poulsen, F.W.; Hendriksen, P.V. Microstructural studies on degradation of interface between LSM–YSZ cathode and YSZ electrolyte in SOFCs. *Solid State Ion.* **2009**, *180*, 1298–1304. [\[CrossRef\]](#)
- Miao, L.; Hou, J.; Dong, K.; Liu, W. A strategy for improving the sinterability and electrochemical properties of ceria-based LT-SOFCs using bismuth oxide additive. *Int. J. Hydrogen Energy* **2019**, *44*, 5447–5453. [\[CrossRef\]](#)
- Danilov, N.; Lyagaeva, J.; Vdovin, G.; Medvedev, D.; Demin, A.; Tsiakaras, P. Electrochemical approach for analyzing electrolyte transport properties and their effect on protonic ceramic fuel cell performance. *ACS Appl. Mater. Interfaces* **2017**, *9*, 26874–26884. [\[CrossRef\]](#)
- Duan, C.; Kee, R.J.; Zhu, H.; Karakaya, C.; Chen, Y.; Ricote, S.; Jarry, A.; Crumlin, E.J.; Hook, D.; Braun, R. Highly durable, coking and sulfur tolerant, fuel-flexible protonic ceramic fuel cells. *Nature* **2018**, *557*, 217–222. [\[CrossRef\]](#)
- Choi, S.M.; An, H.; Yoon, K.J.; Kim, B.-K.; Lee, H.-W.; Son, J.-W.; Kim, H.; Shin, D.; Ji, H.-I.; Lee, J.-H. Electrochemical analysis of high-performance protonic ceramic fuel cells based on a columnar-structured thin electrolyte. *Appl. Energy* **2019**, *233*, 29–36. [\[CrossRef\]](#)
- An, H.; Lee, H.-W.; Kim, B.-K.; Son, J.-W.; Yoon, K.J.; Kim, H.; Shin, D.; Ji, H.-I.; Lee, J.-H. A 5 × 5 cm² protonic ceramic fuel cell with a power density of 1.3 W cm^{−2} at 600 °C. *Nat. Energy* **2018**, *3*, 870–875. [\[CrossRef\]](#)
- Song, Y.; Chen, Y.; Wang, W.; Zhou, C.; Zhong, Y.; Yang, G.; Zhou, W.; Liu, M.; Shao, Z. Self-Assembled triple-conducting nanocomposite as a superior protonic ceramic fuel cell cathode. *Joule* **2019**, *3*, 2842–2853. [\[CrossRef\]](#)
- Steele, B.C. Survey of materials selection for ceramic fuel cells II. Cathodes and anodes. *Solid State Ion.* **1996**, *86*, 1223–1234. [\[CrossRef\]](#)
- Rioja-Monllor, L.; Bernuy-Lopez, C.; Fontaine, M.-L.; Grande, T.; Einarsrud, M.-A. Processing of high performance composite cathodes for protonic ceramic fuel cells by exsolution. *J. Mater. Chem. A* **2019**, *7*, 8609–8619. [\[CrossRef\]](#)
- Zhou, X.-D. Kill Two Problems with One Dual-Ion Cell. *Joule* **2019**, *3*, 2595–2597. [\[CrossRef\]](#)
- Choi, S.; Kucharczyk, C.J.; Liang, Y.; Zhang, X.; Takeuchi, I.; Ji, H.-I.; Haile, S.M. Exceptional power density and stability at intermediate temperatures in protonic ceramic fuel cells. *Nat. Energy* **2018**, *3*, 202–210. [\[CrossRef\]](#)
- Song, X.; Guo, W.; Guo, Y.; Mushtaq, N.; Shah, M.A.K.Y.; Irshad, M.S.; Lund, P.D.; Asghar, M.I. Nanocrystalline Surface Layer of WO₃ for Enhanced Proton Transport during Fuel Cell Operation. *Crystals* **2021**, *11*, 1595. [\[CrossRef\]](#)
- Lu, Y.; Wang, J.; Mushtaq, N.; Yousaf Shah, M.A.K.; Irshad, S.; Rauf, S.; Motola, M.; Yan, S.; Zhu, B. Excellent oxygen reduction electrocatalytic activity of nanostructured CaFe₂O₄ particles embedded microporous Ni-Foam. *Int. J. Hydrogen Energy* **2022**, *47*, 10331–10340. [\[CrossRef\]](#)
- Zhou, X.; Hou, N.; Gan, T.; Fan, L.; Zhang, Y.; Li, J.; Gao, G.; Zhao, Y.; Li, Y. Enhanced oxygen reduction reaction activity of BaCe_{0.2}Fe_{0.8}O_{3-δ} cathode for proton-conducting solid oxide fuel cells via Pr-doping. *J. Power Sources* **2021**, *495*, 229776. [\[CrossRef\]](#)
- Tarutina, L.R.; Lyagaeva, J.G.; Farlenkov, A.S.; Vylkov, A.I.; Vdovin, G.K.; Murashkina, A.A.; Demin, A.K.; Medvedev, D.A. Doped (Nd, Ba) FeO₃ oxides as potential electrodes for symmetrically designed protonic ceramic electrochemical cells. *J. Solid State Electrochem.* **2020**, *24*, 1453–1462. [\[CrossRef\]](#)
- Duan, C.; Tong, J.; Shang, M.; Nikodemski, S.; Sanders, M.; Ricote, S.; Almansoori, A.; O’Hayre, R. Readily processed protonic ceramic fuel cells with high performance at low temperatures. *Science* **2015**, *349*, 1321–1326. [\[CrossRef\]](#) [\[PubMed\]](#)
- Mushtaq, N.; Xia, C.; Dong, W.; Wang, B.; Raza, R.; Ali, A.; Afzal, M.; Zhu, B. Tuning the energy band structure at interfaces of the SrFe_{0.75}Ti_{0.25}O_{3-δ}–Sm_{0.25}CeO₃ heterostructure for fast ionic transport. *ACS Appl. Mater. Interfaces* **2019**, *11*, 38737–38745. [\[CrossRef\]](#) [\[PubMed\]](#)
- Kotomin, E.A.; Mastrikov, Y.A.; Merkle, R.; Maier, J. First principles calculations of oxygen reduction reaction at fuel cell cathodes. *Curr. Opin. Electrochem.* **2020**, *19*, 122–128. [\[CrossRef\]](#)

25. Tatarchuk, T.; Bououdina, M.; Vijaya, J.J.; Kennedy, L.J. Spinel ferrite nanoparticles: Synthesis, crystal structure, properties, and perspective applications. In *International Conference on Nanotechnology and Nanomaterials*; Springer: Cham, Switzerland, 2016; pp. 305–325.
26. Zuo, F.; Wang, L.; Wu, T.; Zhang, Z.; Borchardt, D.; Feng, P. Self-Doped Ti³⁺ enhanced photocatalyst for hydrogen production under visible light. *J. Am. Chem. Soc.* **2010**, *132*, 11856–11857. [[CrossRef](#)]
27. Liu, M.; Lynch, M.E.; Blinn, K.; Alamgir, F.M.; Choi, Y. Rational SOFC material design: New advances and tools. *Mater. Today* **2011**, *14*, 534–546. [[CrossRef](#)]
28. Vøllestad, E.; Strandbakke, R.; Tarach, M.; Catalán-Martínez, D.; Fontaine, M.-L.; Beeaff, D.; Clark, D.R.; Serra, J.M.; Norby, T. Mixed proton and electron conducting double perovskite anodes for stable and efficient tubular proton ceramic electrolyzers. *Nat. Mater.* **2019**, *18*, 752–759. [[CrossRef](#)]
29. Campbell, C.T.; Peden, C.H. Oxygen vacancies and catalysis on ceria surfaces. *Science* **2005**, *309*, 713–714. [[CrossRef](#)]
30. Patade, S.R.; Andhare, D.D.; Kharat, P.B.; Humbe, A.V.; Jadhav, K. Impact of crystallites on enhancement of bandgap of Mn_{1-x}Zn_xFe₂O₄ ($1 \geq x \geq 0$) nanospinels. *Chem. Phys. Lett.* **2020**, *745*, 137240. [[CrossRef](#)]
31. Chen, M.; Paulson, S.; Kan, W.H.; Thangadurai, V.; Birss, V. Surface and bulk study of strontium-rich chromium ferrite oxide as a robust solid oxide fuel cell cathode. *J. Mater. Chem. A* **2015**, *3*, 22614–22626. [[CrossRef](#)]
32. Mantzavinos, D.; Hartley, A.; Metcalfe, I.S.; Sahibzada, M. Oxygen stoichiometries in La_{1-x}Sr_xCo_{1-y}Fe_yO_{3-δ} perovskites at reduced oxygen partial pressures. *Solid State Ion.* **2000**, *134*, 103–109. [[CrossRef](#)]
33. Mueller, D.N.; De Souza, R.A.; Yoo, H.-I.; Martin, M. Phase stability and oxygen nonstoichiometry of highly oxygen-deficient perovskite-type oxides: A case study of (Ba, Sr) (Co, Fe) O_{3-δ}. *Chem. Mater.* **2012**, *24*, 269–274. [[CrossRef](#)]
34. Chandramohan, P.; Srinivasan, M.; Velmurugan, S.; Narasimhan, S. Cation distribution and particle size effect on Raman spectrum of CoFe₂O₄. *J. Solid State Chem.* **2011**, *184*, 89–96. [[CrossRef](#)]
35. Singh, S.; Khare, N. Defects/strain influenced magnetic properties and inverse of surface spin canting effect in single domain CoFe₂O₄ nanoparticles. *Appl. Surf. Sci.* **2016**, *364*, 783–788. [[CrossRef](#)]
36. Zhu, K.; Liu, H.; Li, X.; Li, Q.; Wang, J.; Zhu, X.; Yang, W. Oxygen evolution reaction over Fe site of BaZr_xFe_{1-x}O_{3-δ} perovskite oxides. *Electrochim. Acta* **2017**, *241*, 433–439. [[CrossRef](#)]
37. Wang, Z.; You, Y.; Yuan, J.; Yin, Y.-X.; Li, Y.-T.; Xin, S.; Zhang, D. Nickel-Doped La_{0.8}Sr_{0.2}Mn_{1-x}Ni_xO₃ Nanoparticles Containing Abundant Oxygen Vacancies as an Optimized Bifunctional Catalyst for Oxygen Cathode in Rechargeable Lithium–Air Batteries. *ACS Appl. Mater. Interfaces* **2016**, *8*, 6520–6528. [[CrossRef](#)]
38. Oh, N.K.; Kim, C.; Lee, J.; Kwon, O.; Choi, Y.; Jung, G.Y.; Lim, H.Y.; Kwak, S.K.; Kim, G.; Park, H. In-situ local phase-transitioned MoSe₂ in La_{0.5}Sr_{0.5}CoO_{3-δ} heterostructure and stable overall water electrolysis over 1000 hours. *Nat. Commun.* **2019**, *10*, 1723. [[CrossRef](#)]

Disclaimer/Publisher’s Note: The statements, opinions and data contained in all publications are solely those of the individual author(s) and contributor(s) and not of MDPI and/or the editor(s). MDPI and/or the editor(s) disclaim responsibility for any injury to people or property resulting from any ideas, methods, instructions or products referred to in the content.